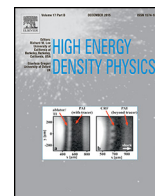




ELSEVIER

Contents lists available at ScienceDirect

High Energy Density Physics

journal homepage: www.elsevier.com/locate/hedp

X-ray opacity measurements in mid-Z dense plasmas with a new target design of indirect heating



M. Dozières^{a,*}, F. Thais^a, S. Bastiani-Ceccotti^b, T. Blenski^a, J. Fariaut^d, W. Fölsner^c,
F. Gilleron^d, D. Khaghani^e, J.-C. Pain^d, C. Reverdin^d, F. Rosmej^f, V. Silvert^d, G. Soullié^d,
B. Villette^d

^a CEA, IRAMIS, LIDyL, Saclay, F-91191 Gif-sur-Yvette, France^b LULI, École Polytechnique, CNRS, CEA, UPMC, F-91128 Palaiseau, France^c Max-Planck-Institut für Quantenoptik, 85748 Garching, Germany^d CEA, DAM, DIF, F-91297 Arpajon, France^e EMMI, GSI Helmholtzzentrum, Darmstadt, Germany^f LULI, Sorbonne Universités UPMC Univ Paris 06, École Polytechnique, CNRS, CEA, F-75005 Paris, France

ARTICLE INFO

Article history:

Received 4 August 2015

Accepted 5 August 2015

Available online 12 August 2015

Keywords:

Laser produced plasmas

X-ray absorption spectroscopy

Opacity codes

Radiative hydrodynamic simulations

ABSTRACT

X-ray transmission spectra of copper, nickel and aluminum laser produced plasmas were measured at the LULI2000 laser facility with an improved target design of indirect heating. Measurements were performed in plasmas close to local thermodynamic equilibrium at temperatures around 25 eV and densities between 10^{-3} g/cm³ and 10^{-2} g/cm³. This improved design provides several advantages, which are discussed in this paper. The sample is a thin foil of mid-Z material inserted between two gold cavities heated by two 300J, 2 ω , nanosecond laser beams. A third laser beam irradiates a gold foil to create a spectrally continuous X-ray source (backlight) used to probe the sample. We investigate 2p–3d absorption structures in Ni and Cu plasmas as well as 1s–2p transitions in an additional Al plasma layer to infer the in-situ plasma temperature. Geometric and hydrodynamic calculations indicate that the improved geometry reduces spatial gradients during the transmission measurements. Experimental absorption spectra are in good agreement with calculations from the hybrid atomic physics code SCO-RCG.

© 2015 Elsevier B.V. All rights reserved.

1. Introduction

Radiative properties are of great interest to probe and understand hot and dense matter such as laser-produced plasmas. One way to study these properties is absorption spectroscopy, which gives access to static and dynamic properties of highly charged ions in plasmas. Moreover, opacity is essential for the calculation of the radiative transfer in hot and dense plasmas encountered in astrophysics and inertial confinement fusion. Calculation of photo-absorption coefficients is a difficult task because of the potentially large number of electronic configurations to be taken into account and interactions between them. Therefore, the benchmarking of opacity codes by comparison to experimental data is of paramount importance. Several opacity measurements have been performed on laser facilities in conditions close to local thermodynamic equilibrium (LTE) using the point-projection backlighting techniques [1]. Absorption measurements require careful target design and precise experimental techniques to obtain data with sufficient spectral and possibly spatial resolution. In the last few decades some experiments

have been performed in the X-ray range with indirect target heating [2,3]. We present here an experiment performed at the LULI2000 facility with a new indirect heating target design as explained below. The target samples are heated by quasi-Planckian radiations at temperatures around 20–30 eV using the X-ray emitted by two laser-irradiated gold cavities. For these conditions the plasmas are close to LTE at high density. This assumption is appropriate considering the laser parameters and the use of the “sandwich” type samples, which are surrounded, i.e., tamped, by two layers of carbon in order to control and limit the plasma expansion. A gold plasma backlight is generated and its radiation is used to probe the studied plasma. In the X-ray range the absorption structures we are interested in are 2p–3d transitions of the mid-Z elements copper and nickel as well as the 1s–2p transitions of aluminum. X-ray spectra are recorded by a high-resolution spectrometer over a wide spectral range of 8–18 Å. Our goal is to simultaneously measure the XUV opacities and the 2p–3d X-ray absorption structures and to use the latter as a temperature diagnostic. In medium-Z plasmas the XUV radiative properties in the 50–150 eV spectral region are often dominated by $\Delta n = 0$ transitions. The electronic states involved in these transitions may have partially overlapping wave functions, leading to high absorption and emission of radiation. Moreover the emission and absorption cross sections of $\Delta n = 0$ transitions are highly

* Corresponding author. CEA, IRAMIS, LIDyL, Saclay, F-91191 Gif-sur-Yvette, France.
E-mail address: maylis.dozieres@cea.fr (M. Dozières).

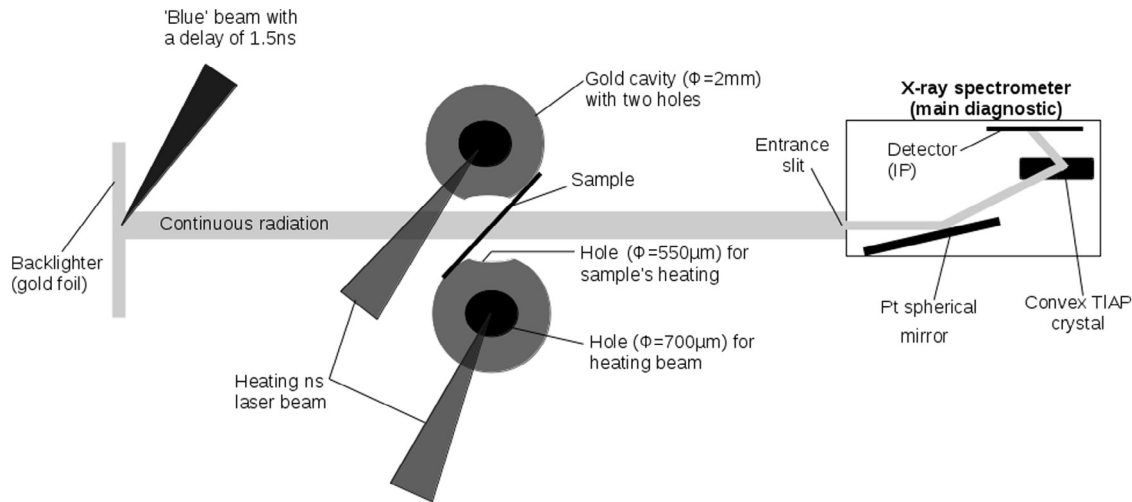


Fig. 1. Setup of the absorption measurement showing the new target design and the main spectrometer.

sensitive to plasma temperature. The 2p–3d transitions in the X-ray range and the XUV 3p–3d transitions ($\Delta n = 0$) involve the same subshells 3p and 3d. The difference is that, in the second case the 3p is not a spectator subshell but an active one. Both the 2p–3d (X-rays) and 3–3 (XUV) absorption structures are very sensitive to the population of the 3p subshell but in different ways. In the X-ray case, a change in the electronic temperature impacts mainly the 2p–3d spectral position, whereas in the XUV case it will affect mainly the strength of the absorption. The measurement of the position of the 2p–3d transition structures can thus be used as a temperature diagnostic during the measurement of the 3–3 transition structures. Using comparisons with opacity codes, these measurements offer two different approaches to determine the electronic temperature. Here we present here results in the X-ray range, which represent the first step of our project. In the next sections we show the experimental setup of the X-ray measurements, the new target design, hydrodynamic simulations of the target and some experimental spectra obtained for comparison to atomic-physics calculations performed with the SCO-RCG code.

2. Experimental setup

2.1. Description

The experiment took place at the LULI2000 Nd:glass laser facility, using a three-beam configuration. Two main high energy, 1.5 ns duration laser beams (“pump” beams) are used to irradiate two gold cavities yielding approximately Planck radiation that are used, in turn, to heat a multi-layer foil on each side. A third 1.5 ns duration laser beam, the “probe” beam, irradiates a gold foil creating a backlight with a delay of 1.5 ns with respect to the rising edge of the two high energy beams. This third beam creates a radiative source to probe the sample foil. This source was previously tested and found to be sufficiently spectrally continuous with a homogeneous global intensity for our need. The two main nanosecond beams are frequency-doubled ($0.526 \mu\text{m}$) for better X-ray conversion efficiency, with a 2ω energy between 300 and 350 J for each beam. The “probe” beam, also frequency-doubled, delivers around 20 J on the backlight target. A schematic experimental set-up of main diagnostic and target design is presented in Fig. 1.

Each nanosecond heating beam is focused on the laser entrance hole of the cavity using a 1600 mm focal length lens coupled with a random phase plate (RPP), yielding a $450 \mu\text{m}$ diameter smoothed focal spot on the rear wall of the cavities. On the other

hand, the “probe” beam is focused by a 500 mm focal length lens providing a $20 \mu\text{m}$ diameter focal spot. The pulse duration of all the laser beams is 1.5 ns. Each cavity has one laser entrance hole of $\Phi = 700 \mu\text{m}$ which is larger than the focal spot and another hole of $550 \mu\text{m}$ diameter that is used to heat the samples. One kind of sample foil consists of a pure metal layer surrounded by two layers of carbon ($15 \mu\text{g}\cdot\text{cm}^{-2}$ areal mass). The second type has an additional layer of aluminum (around $10 \mu\text{g}\cdot\text{cm}^{-2}$ areal mass) inserted between the metal and the carbon layers. The sample list is summarized in Table 1. It is important to note that, in transmission calculations, the areal masses in Table 1 have been multiplied by $\sqrt{2}$ to take into account the sample’s angle of 45° (see Fig. 2) during radiography.

The main diagnostic is a spectrometer with two independent tracks, which allows one to simultaneously detect X and XUV spectra. The X-ray channel consists of an entrance slit, a platinum-coated spherical mirror and a TIAP convex crystal. The dimensions of the mirror are 120 mm length, 40 mm width and a curvature radius of 8080 mm. The spectrometer is deployed at a grazing incident angle (1.5°) to provide good reflectivity while removing the hard X rays [4]. Finally, the signal focused on the TIAP convex crystal is spectrally dispersed over a wide energy range in accordance with Bragg’s law. With a length of 60 mm, a width of 20 mm and a curvature radius of 100 mm this crystal provides a spectral range of 690–1550 eV and an average spectral resolution of about 400. Time-integrated spectra are detected on a photostimulated Imaging Plate (IP) Fuji BAS-TR [5]. IPs are sensitive to X-rays because their cut-off wavelength is above 200 nm implying that they do not record the laser and visible light coming from reflections and other extralight. The goal of this main spectrometer is to measure the absorbed spectrum, i.e., the measurement of the intensity, I , and the unperturbed backlight spectrum giving a measurement of the incident backlight intensity, I_0 . Thus, we can determine the transmission spectra as the ratio I/I_0 . It is important to note that during this

Table 1
Summary of samples’ characteristics.

	Shoot #64	Shoot #71	Shoot #69	Shoot #72
Materials	C/Al/ Ni/Al/C	C/Ni/C	C/Al/Cu/Al/C	C/Cu/C
Thicknesses (nm)	70/38/11/38/70	70/28/70	70/38/12/38/70	70/22/70
Areal masses ($\mu\text{g}/\text{cm}^2$)	15/10/10/10/15	15/25/15	15/10/11/10/15	15/20/15

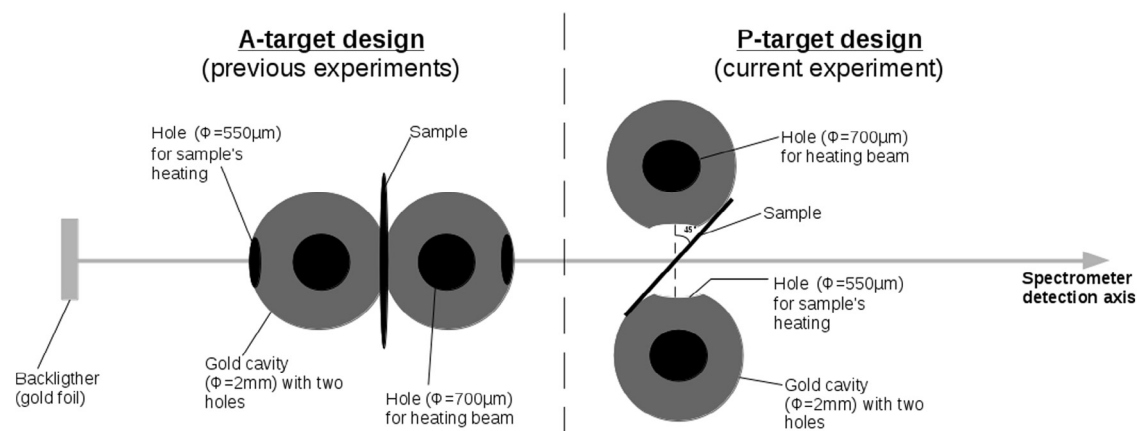


Fig. 2. Geometrical layout of the two types of target setup.

campaign I and I_0 are measured separately, using different shots at similar experimental conditions. Additional diagnostics are also used to characterize plasmas created in the cavities, the backlight target and the sample. A time-integrated X-ray pinhole camera provides a measure of the three focal spots and indicates the global alignment. Two absolutely calibrated, time-resolved, X-ray broadband spectrometers called “DMX” are added to measure the radiation temperature of the cavities. Each DMX consists of several channels with different filters coupled with X-ray vacuum diodes to deduce the X-ray emission from 100 eV to approximately 5 keV [6]. The filters are carefully chosen to obtain adequate coverage of the energy band for each channel, which will allow reconstruction of the entire spectrum. The measure of radiation temperatures of the cavities is about 45–50 eV. Finally, to observe the backlight emission for each shot a spherical quartz crystal (FSSR) spectrometer is implemented. This spectrometer, based on spherical mirror focusing and Bragg’s law, has a high spectral resolution, i.e., ~ 3000 , and provides a spectrum in the 1550–1700 eV spectral range.

The goal of this experiment is to create a plasma of mid-Z element near LTE in order to study its absorption between 800 and 1600 eV. So we employ gold cavities to produce an approximately Planckian radiation applied to heat samples. This indirect heating method allows us to consider that the plasma is brought close to LTE [7]. Furthermore, the use of the 2ω laser energy to irradiate cavities increases the absorption rate of the laser energy and limits the generation of suprathermal electrons allowing us to have a more intense and more homogeneous radiation source on the sample. The elemental composition of the backlight foil and cavities had been validated during preliminary experiments on the EQUINOX facility (CEA, France) where gold had been chosen rather than other materials like Cu, Mo, Zr, etc. Gold has been shown to be the element that converts the laser flux most efficiently to X-rays, leading to the most spectrally continuous emission spectra [8]. Considering the 1.5 ns pulse duration for the two heating beams, we have chosen to apply a delay of 1.5 ns to the “probe” beam to optimize the hydrodynamic parameters at the time of the measurement, to probe a dense and hot plasma with minimal spatial gradients. In fact at later time, the temperature and density decrease and at earlier time gradients are too important. One can notice that the pulse duration of the “probe” beam is also of 1.5 ns because the three laser beams on LULI2000 facility must have the same pulse duration. So the duration, which is identical for the three laser beams, results from a compromise between the energy needed to heat the cavities and the requirement for the duration of the “probe” beam to be as short as possible.

Finally, the last parameter that is used to control the plasma conditions is the areal mass of the two carbon layers surrounding the

samples. With these “sandwich” targets, in principle, we also limit the plasma expansion [9] in order to reduce temperature and density gradients while maintaining a relatively high density. For each family of samples, two shots are recorded at similar conditions by the main spectrometer. One shot is realized with the sample foil between cavities, i.e., the real transmission or the “I” measurement and the other one is realized without the sample foil and the cavities, i.e., which is reference or “ I_0 ” measurement. One can notice that making separate measurements of I and I_0 increases the risk of discrepancies when compared to an ideal case where both measurements were performed simultaneously. The main source of possible discrepancies is the shot-to-shot fluctuations of the laser parameters. For this reason, we implemented the FSSR spectrometer. Recording the backlight emission on each shot allows us to choose the reference shot (I_0) in order to recover as close as possible the backlight conditions observed during the absorption shot (I). So with this additional spectrometer we are more confident that we have reproducible absorption spectra.

2.2. Target design

About ten opacity experiments were realized by our team during last decades, using different indirect heating target designs. The first experiments were performed with the sample attached on one gold cavity [10,11]. Later, we moved to a scheme in which the sample was squeezed between two gold cavities. In this scheme, the cavities were aligned with the backlight and the spectrometer, i.e., they were on the detection axis. Throughout this paper, this configuration is called the A-target design (see Fig. 2). In this setup the self-emission radiation of the cavities is also recorded on the detector, and this greatly complicates the analysis of the absorption spectra. In the experiment presented here, the cavities are placed on an axis perpendicular to the detection axis. This new configuration is called the P-target design (see Fig. 2). In this case, the self-emission of the two cavities is removed from detection axis of the spectrometer, giving lower noise on the spectra in comparison with previous experiments. In addition, placing the cavities away from the line of sight allows us to avoid issues associated to the filling of the cavities with plasmas. In fact the plasma inside the cavities takes time to come into the line of sight of the measurement axis and so disturb the detection. It is therefore necessary to take into account this phenomenon with the A-target design while this problem is avoided with the P-type target.

From an experimental point of view, the P-target design leads to easier alignment, as it is only necessary to place the cavities as close as possible to the sample. Instead, with the A-target design

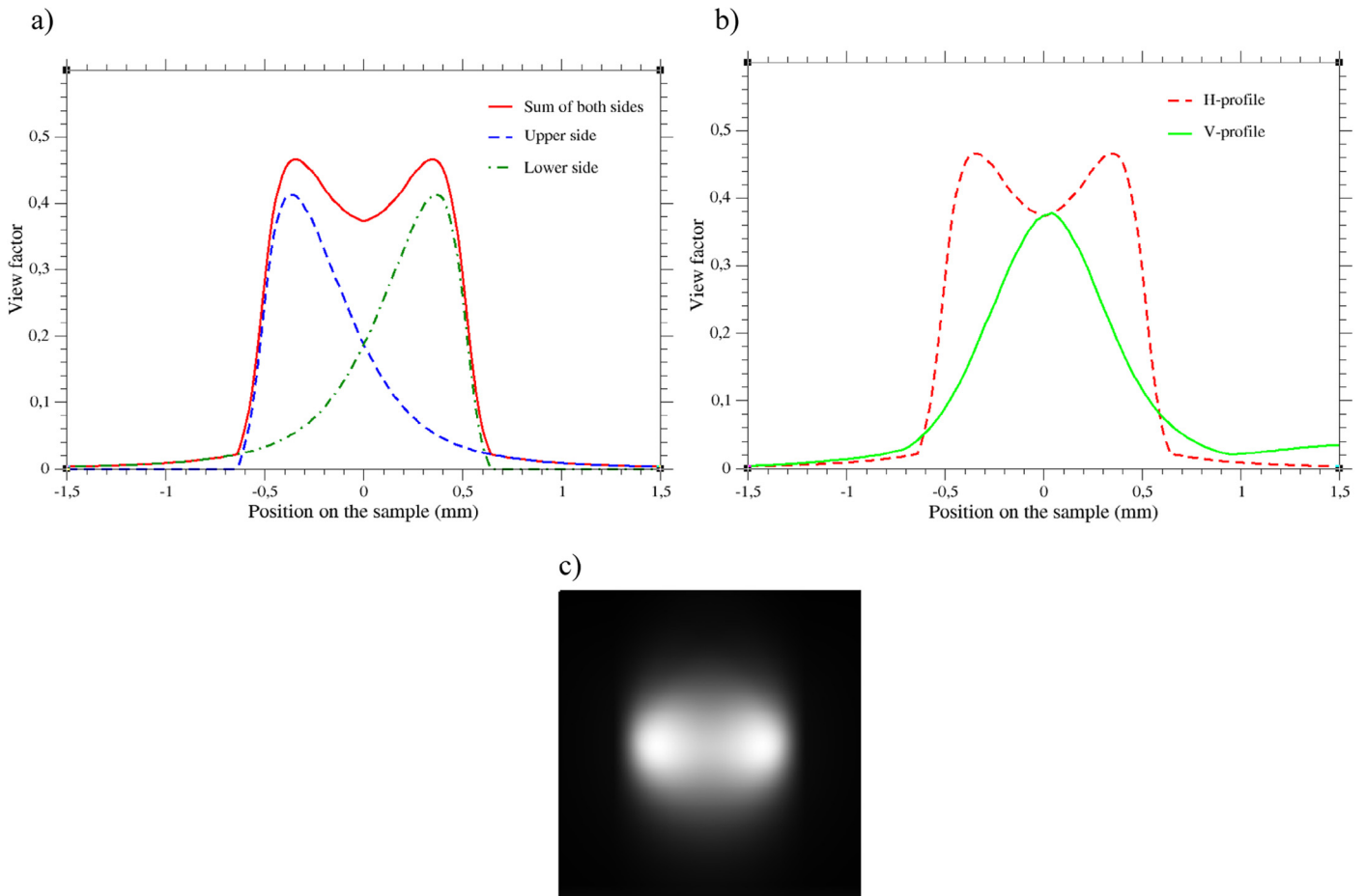


Fig. 3. (a) View factor horizontal irradiance profiles of the sample in the P-target design. (b) Horizontal and vertical profiles of irradiance in P-target design. (c) Image of both sides sample's irradiance in P-target design.

we needed to precisely align four holes on the same axis (the detection one). So the alignment of the P-target saves time and reduces the risks of losing some part of the signal due to possible misalignment of the cavities. The disadvantage of the P-target design is the less efficient heating, as the cavities are further from the sample. Nevertheless, the irradiance calculations made with the “View Factor” model (see Appendix) show that the heating in the P-target is still quite homogeneous (see Fig. 3c), even if the region of greater irradiance on each side (upper and bottom) is not centered, but slightly shifted (see Fig. 3a). This remark affects only the horizontal profile of the sample, the irradiance in the vertical direction being maximum at the center of the sample (see Fig. 3b).

Taking into account the 2 mm spectrometer entrance, and the distances between the slit and the sample and between the sample and the backlight, 133 and 5 mm, respectively, we probe restricted area of about $70\ \mu\text{m}$ around the center of the sample. Thus, to have the maximum irradiance in the sample center, and the best heating, cavities have been slightly shifted away from the sample along the spectrometer axis. Then the positions of the maximum intensity of the irradiance from each cavity are spatially superposed on the sample center, as shown in Fig. 4. With this adjustment, we obtain irradiance approximately two times stronger in the center of the foil. Nevertheless, it remains lower than the irradiance obtained in the A-target geometry, leading to a lower sample temperature. We counterbalanced this by an increase of the energy of the heating laser beams.

In conclusion, in our new experiment design two points are important for the study of the plasma: the homogeneity of the heating and the electronic temperature that can be achieved. In the new P-target geometry, the first point is acceptable because of the homogeneous irradiance, while the second point can be addressed by putting more laser energy into the two cavities.

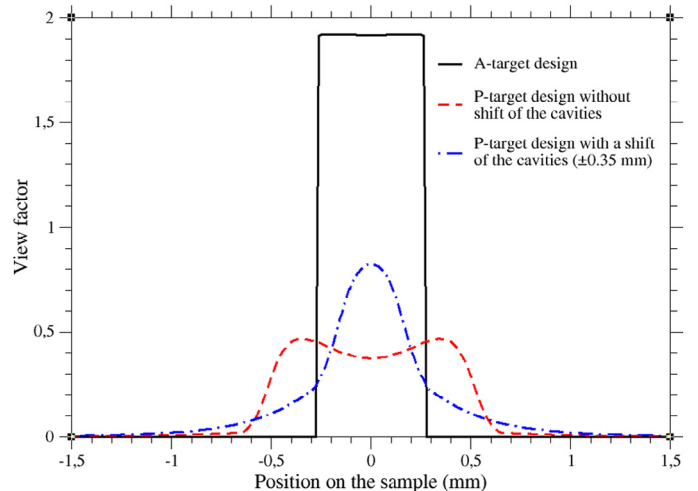


Fig. 4. Irradiance profiles on the sample for different target geometries.

3. Data processing and results

The first step is to linearize the data obtained from the scan of the imaging plate. The scanner operates with a step size of $25 \times 25 \mu\text{m}^2$ and provides non-linear data. To recover pixel values proportional to photon energy, we apply the standard formula supplied by the scanner manufacturer and obtain linear data in PSL (PhotoStimulated Light) [5]. We then remove the background on the image, and plot the spectra by integrating the pixel values.

In order to calibrate the spectral dispersion in energy as a function of the position of the detector, several shots have been performed on an aluminum sample to detect well-known X-ray emission lines, which are used in addition to the theoretical dispersion function of the spectrometer. The spectral resolution is estimated to about 2 eV. Next, the spectrometer total sensitivity is taken into account to correct the intensity of spectra. This sensitivity contains spectral resolution dE/dX , image plate's sensitivity, spectral and spatial spectrometer's view of the source, the filters' transmission ($2 \mu\text{m}$ of Mylar and $0.15 \mu\text{m}$ of Al) and Pt mirror reflectivity. This is presented in Fig. 5 for the energy range of interest.

Finally, a sliding average over 10 pixels is made for every point to smooth the noise without changing the strength of absorption structures. This smoothing respects the resolution and does not impact the significant absorption structures.

This processing is applied both to the absorption spectra and the backlight spectra before calculating the ratio between them that yields the resulting transmissions. As previously stated, to choose the backlight shot to associate with a given absorption shot we use data collected with the spherical quartz spectrometer (FSSR). As an example of the procedure, we show in Fig. 6 four backlight spectra obtained with similar probe beam parameters. One of them (#71) is obtained during an absorption shot, the others are obtained during “backlight only” shots.

We note that the spectra show very similar spectral characteristics, both in shape and in relative intensity, except for shot #70. Spectra obtained in shots #60 and #68 are very close to the spectrum recorded in the absorption shot (#71), so we choose to calculate the transmission for this shot using each backlight spectra recorded in shots #60 and #68 to finally make the final arithmetic average value of this two transmission spectra. The same procedure is used for each absorption shot and the measured spectral transmission for some of them are presented in Fig. 7.

Absorption structures are clearly visible on these spectra. They correspond to the 2p–3d transitions for nickel and copper and to the 1s–2p transitions for aluminum. Fig. 7b and d shows copper transmission obtained with two different sample areal masses

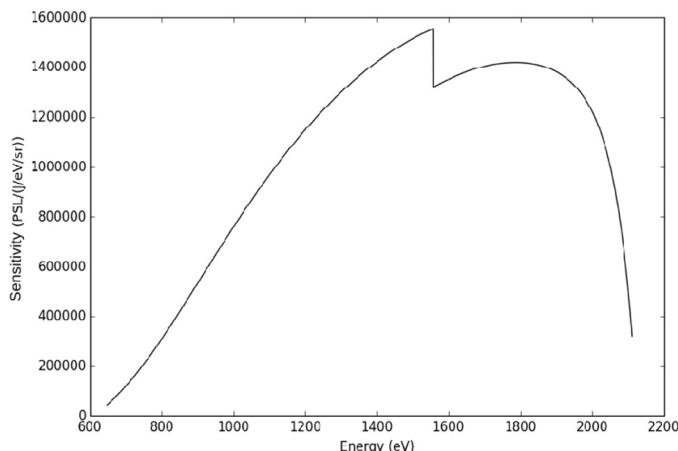


Fig. 5. Total response function of the spectrometer as a function of the energy.

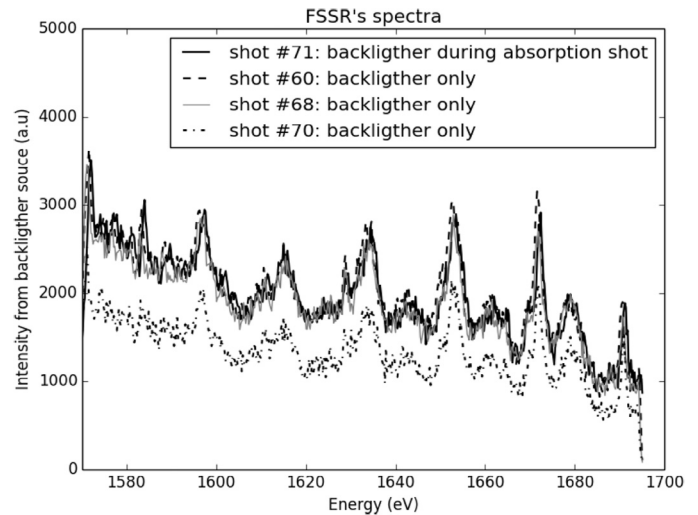


Fig. 6. Comparison between a backlight spectrum recorded in absorption shot #71 (black solid line) and three backlight spectra (dashed, dot dashed and gray solid lines) obtained in shots dedicated to I_0 measurement.

($10 \mu\text{g}/\text{cm}^2$ and $20 \mu\text{g}/\text{cm}^2$, respectively). In both cases, the structures corresponding to 2p–3d and 2p–4d transitions are present, but they are more apparent in the case of the sample with the larger mass. Moreover, the spin-orbit splitting of the 2p–3d and 2p–4d transitions is also more apparent for the thicker sample. Same consideration apply for the nickel transmission spectra shown in Fig. 7a and c. Also, we can distinguish clearly the 1s–2p aluminum structures in spectra from shots #64 and #69, which can play here a role of thermometer. In fact, as it is well-known, spectral calculations for Al are much more accurate than for mid- and high-Z elements. Thus, they can be used as diagnostic of the electron temperature. The temperature deduced in this way is then used as input for nickel and copper calculations of the absorption structures.

4. Hydrodynamic calculations

The hydrodynamic simulations of the cavity heating were performed with the FC12 2D Lagrangian radiation hydrodynamics code [12] in cylindrical geometry. We used multi-group Monte Carlo transport to simulate the radiative energy within the cavity, coupled to high-quality LTE opacity tables that use fast non-LTE corrections [13,14]. The laser heating of both cavities was treated by a ray-tracing algorithm accounting for the propagation, refraction and collisional absorption of the laser flux. We took into account an estimate of the laser energy inside each cavity and consider a 1.5 ns square laser pulse. The focal spot was described by a $400 \mu\text{m}$ diameter super-Gaussian shape.

These 2D simulations of the cavity heating give the input for the 2D hydrodynamic calculations of the sample. As a first step, we consider a sample in LTE irradiated by the calculated Planckian radiative temperature coming out of each cavity. The simulations of the hydrodynamics of the sample have been performed with the calculated temperature profile, taking into account the uncertainties on laser energy deposition in the cavity. These calculations allow one to predict the thermodynamic conditions of the sample when it is irradiated by the backlight 1.5 ns after the heating laser pulse.

The electron density and temperature profiles at four different times are given in Fig. 8, corresponding to the duration of the backlight (1.5–3 ns). We can see that the peak electron temperature reached in the copper and the nickel foils during the backlight pulse is about $T_e \sim 25\text{--}35 \text{ eV}$ with mass density $\rho \sim 10^{-3}\text{--}10^{-2} \text{ g}\cdot\text{cm}^{-3}$. It is important to note that these calculations depend on the laser energy

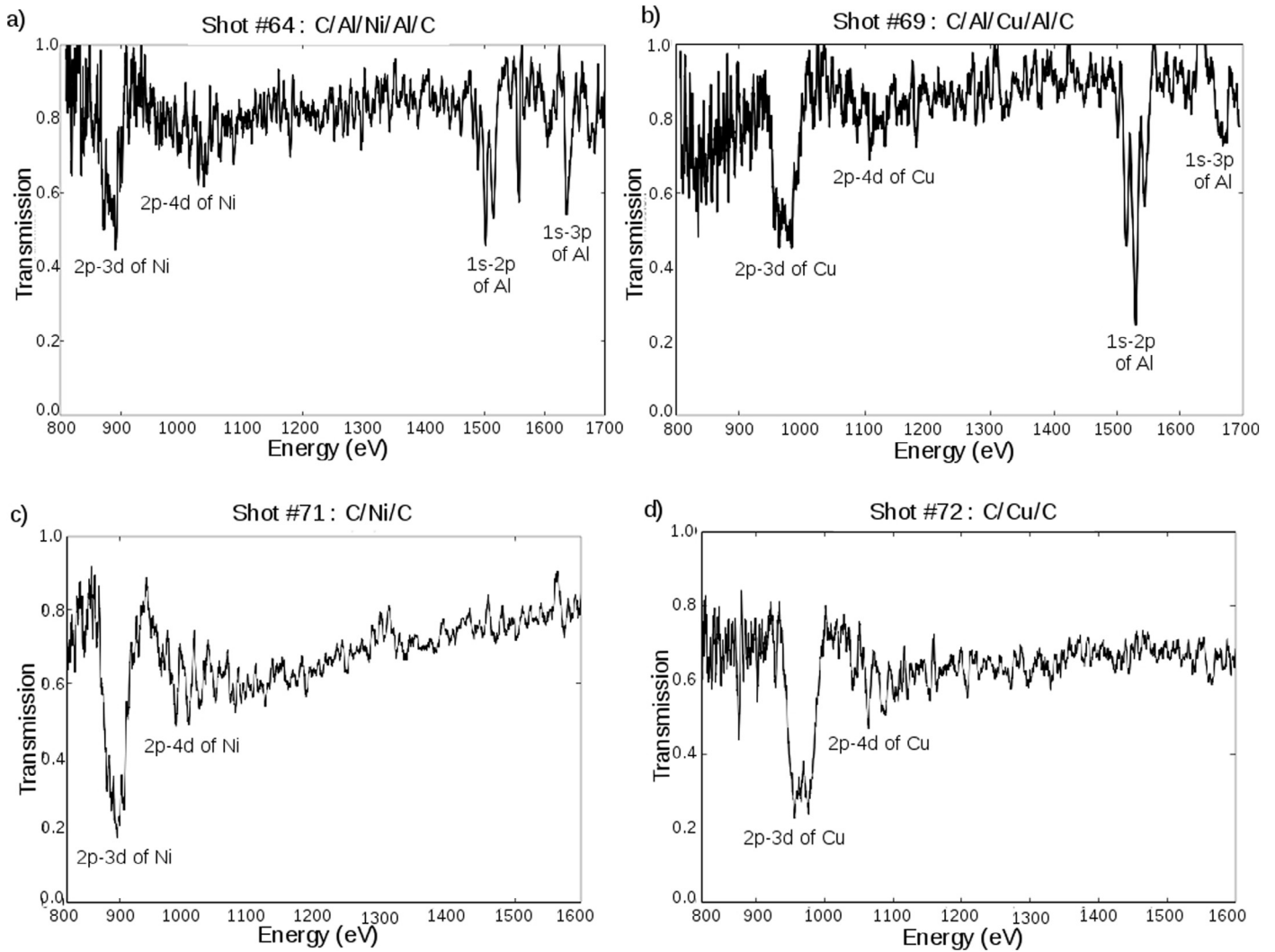


Fig. 7. Absorption spectra of different samples: (a) Ni ($10 \mu\text{g}/\text{cm}^2$) sandwiched between two layers of Al ($10 \mu\text{g}/\text{cm}^2$), (b) Cu ($10 \mu\text{g}/\text{cm}^2$) sandwiched between two layers of Al ($10 \mu\text{g}/\text{cm}^2$), (c) Ni ($25 \mu\text{g}/\text{cm}^2$) and (d) Cu ($20 \mu\text{g}/\text{cm}^2$). Every sample is tamped with two layers of carbon ($15 \mu\text{g}/\text{cm}^2$) on both sides.

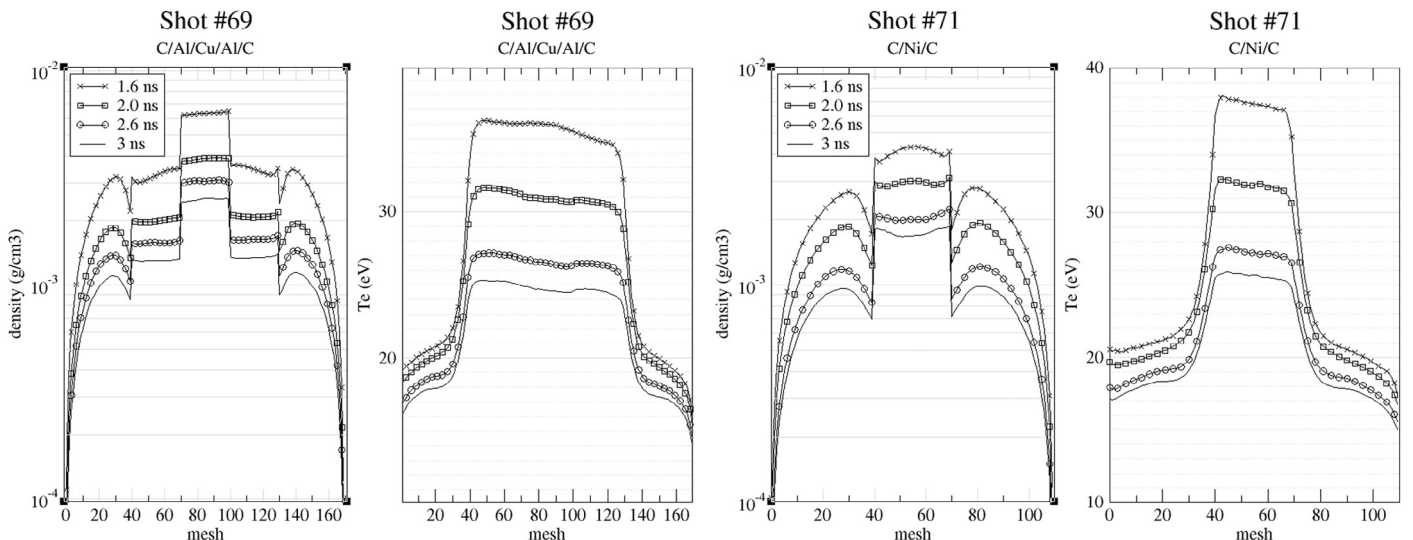


Fig. 8. Density and electronic temperature at different probe times for the shots #71 and #69 calculated with FCI2 code.

inside the cavities, and that these values are just estimated. As a consequence, these profiles provide only an order of magnitude for the electronic temperature and density. Furthermore and as expected, we can see that spatial gradients in copper and nickel are reduced while temporal variations are stronger.

5. Comparison with atomic physics code

Results obtained during this campaign have been compared to calculations made by the atomic physics code SCO-RCG [15,16], which is a hybrid opacity code combining statistical and detailed (fine-structure) modeling of atomic properties and spectra. The *nlj* orbitals are treated individually up to a certain limit beyond which they are gathered in a single super-shell. The grouped orbitals are chosen so that they weakly interact with inner orbitals. When there is at least one electron in this supershell, the resulting electron structure is a super-configuration; otherwise it is an ordinary configuration. The code uses several criteria, e.g., the Boltzmann probability, number of successive excitations, etc. in order to decide which set of configurations or super-configurations must be taken into account. All calculations (detailed or not) are performed with wavefunctions computed in the super-configuration formalism, based on the density-functional theory at finite temperature, to ensure a consistent description of the plasma-environment effects in the code [17]. Whenever possible, ordinary configurations are split into levels by diagonalizing the Hamiltonian matrix in a method adapted from

Cowan's code [18] and the arrays of lines between two detailed configurations are computed in the intermediate coupling. Otherwise, configurations are treated statistically, giving rise to unresolved transition arrays represented in the UTA (Unresolved Transition Arrays) or SOSA (Spin-Orbit Split Arrays) formalisms. The spectral contribution due to the super-configurations may be calculated either statistically by Super Transition Arrays (with large unresolved structures) or in a more detailed way using a generalization of the Partially Resolved Transition Array approach [19]. In the latter case, the supershell is first purposely omitted in order to perform fine-structure calculations (under the same conditions as mentioned above) with the wavefunctions of the genuine super-configuration. The contribution of the supershell is then taken into account as an additional Gaussian width to this reduced detailed transition array [20].

As we can see in Fig. 9, calculations are in good agreement with the experimental data. In these calculations, the density is assumed to be $10^{-2} \text{ g.cm}^{-3}$ for each case and the total transmission is obtained by multiplying the transmission of each layer of different *Z* elements. In the present calculated transmissions, the statistical part of the opacity (UTA, SOSA, STA) is negligible compared to the detailed one. The position of each 2p–3d absorption feature is accurately reproduced by calculations for a given temperature. Table 2 contains the different temperatures used to determine the best fit of the experimental spectra in the four cases.

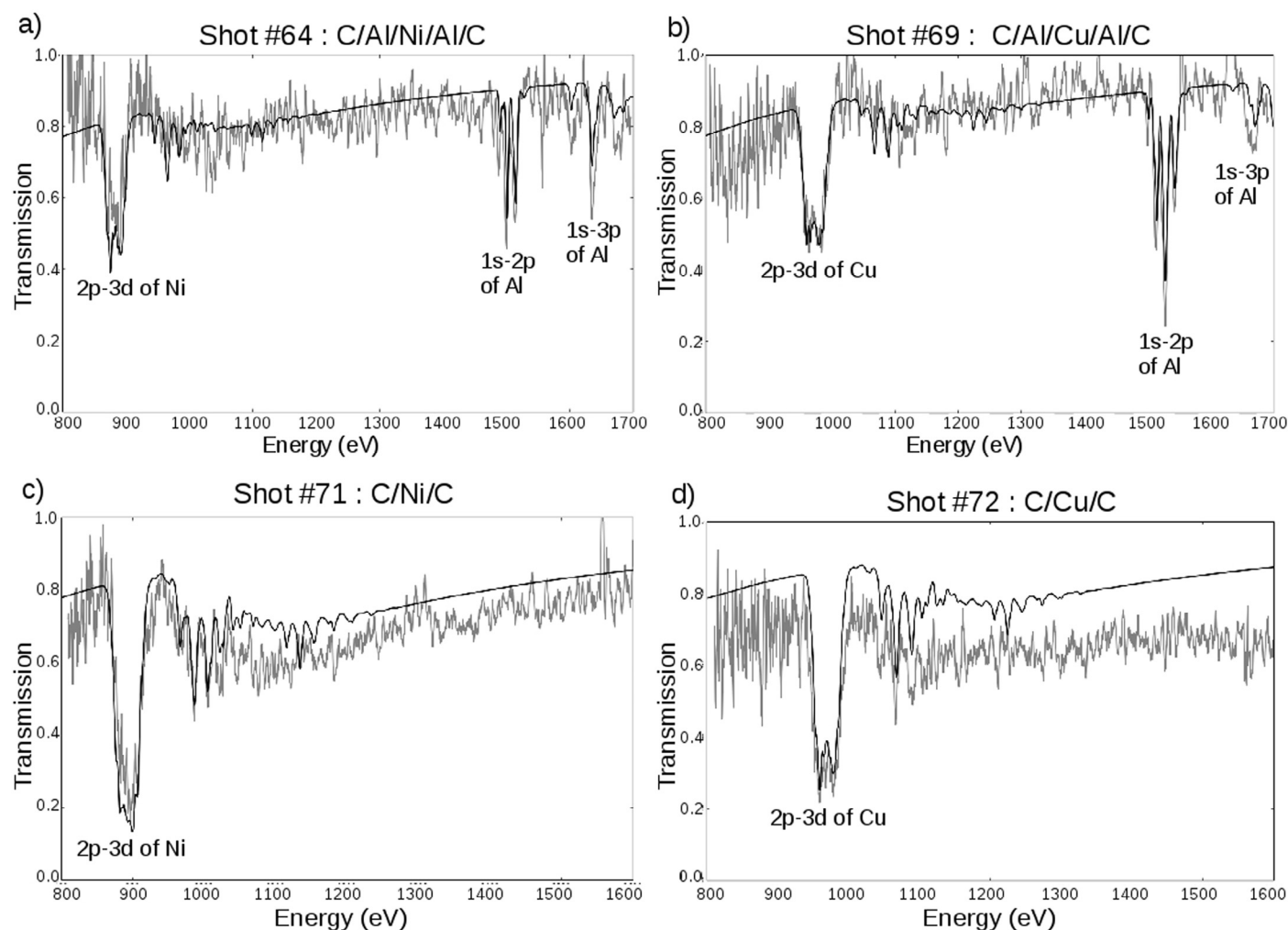


Fig. 9. SCO-RCG calculations (black curves) compared to experimental data (gray curves) for four shots with different elements.

Table 2

Temperature of each layer in the four samples.

Shot #64: C/Al/Ni/Al/C	Shot #69: C/Al/Cu/Al/C
C: 20 eV	C: 20 eV
Al: 23 eV	Al: 34 eV
Ni: 20 eV	Cu: 27 eV
Shot #71: C/Ni/C	Shot #72: C/Cu/C
C: 20 eV	C: 20 eV
Ni: 26 eV	Cu: 25 eV

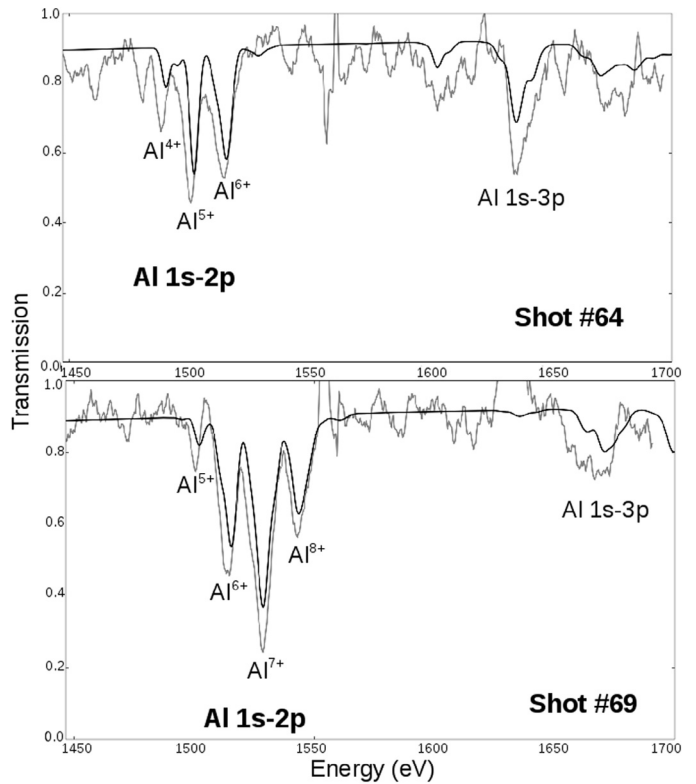
It has been assumed in these calculations that an approximate density, identical for every case, because the position of the 2p–3d structures is much more sensitive to temperature than to density [21]. Actually, when the temperature increases the excited states are more populated by electrons. This implies more fluctuations of bound subshell occupations and leads to a multiplication of the configurations contributing to the 2p–3d transition, including lines slightly shifted in frequency. This shift is due to the variation of the number of spectator electrons in different subshells. However, only the strength of the 1s–2p transition of aluminum is dependent on the temperature, not its position. Hence, aluminum structure can be used as a thermometer to estimate the plasma temperature because the aluminum absorption structures of K-shell transitions (being composed from different charge states) are really sensitive to the temperature.

We observe in Fig. 9a the absorption due to Al⁴⁺–Al⁶⁺ and in Fig. 9b, the absorption structures due to Al⁵⁺–Al⁸⁺. The reason for this is quite obvious, as the temperature is higher, and the ionization is more important. In addition we observe that the spin-orbit splitting for the copper and nickel structures is slightly visible as expected from the theory [22]. So the SCO-RCG code accurately reproduces the position, the shape and the strength of the 2p–3d absorption structure of copper and nickel. However, the absolute transmission of Al structures seems to be underestimated by the code (see Fig. 10).

One can also notice that, for shots #64 and #69, the absolute value of the general transmission is very well fit by SCO-RCG calculations, while in the cases of the shots #71 and #72 the agreement should be improved. However, the absolute value of the transmission is not really significant in this experiment, due to the separated measurements of I and I₀ (see Section 2.1).

6. Conclusion and perspectives

We have successfully tested a new target design of indirect heating, which provides more reproducible and very low noise X-ray spectra, while saving experimental time. We have recorded with good accuracy 2p–3d X-ray transitions of copper and nickel laser produced plasmas at electron temperature of about 20–30 eV and a density of about 10⁻² g.cm⁻³. The hydrodynamic calculations have confirmed that density and electron temperature gradients were reduced with this new target design, which further ensures good homogeneity and heating of the sample. The experimental spectra were compared to the hybrid code SCO-RCG and the calculations are in good agreement. Furthermore, we have shown that the temperature diagnostic based on extra Al layers in the sample is an additional tool to validate both hydrodynamic and opacity codes. It also permits one to have a deeper insight into the sample heating. Finally, we could observe in the spectra the presence of 2p–4d transitions of copper and aluminum for the thicker foils. That allows us to dedicate a study of these transitions with more confidence for future experiments in which the main goal will be the simultaneous measurement of X-ray and XUV spectra.

**Fig. 10.** Zoom on the Al structures for shots #64 and #69.

Acknowledgements

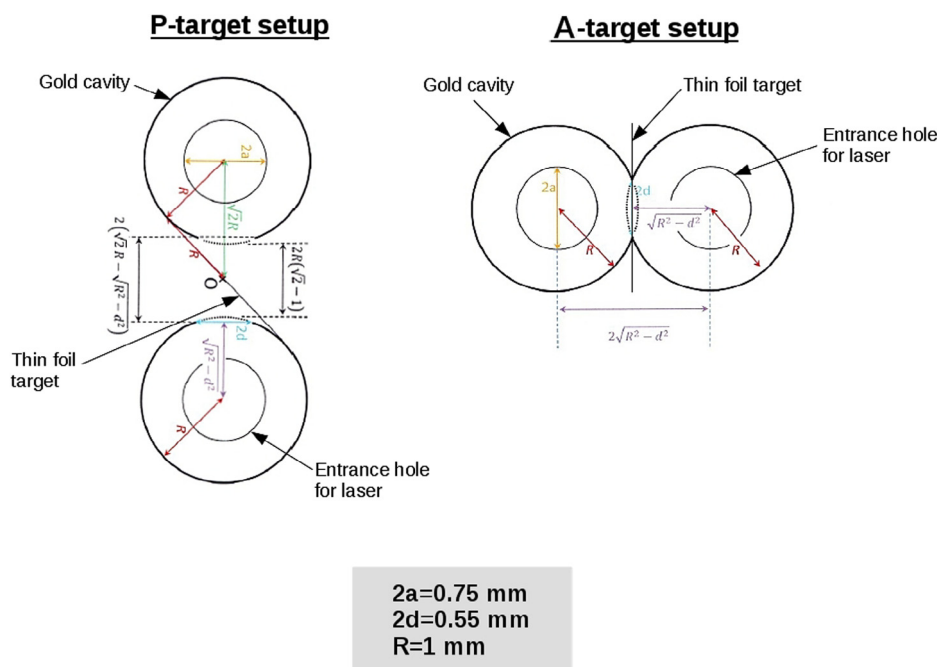
The authors would like to acknowledge the invaluable support of the LULI facility operations staff and the on-site technical teams. On the other hand, we appreciated the quality of the samples made by the “Groupe Cibles - Institut de Physique Nucléaire d’Orsay - France”. This work has been carried out within the ToIFE project in framework of the EUROfusion Consortium and has received funding from the EURATOM research and training program 2014–2018 under grant agreement No 633053. The views and opinions expressed herein do not necessarily reflect those of the European Commission. The support from the French National Agency of Research through the LabEx PALM (ANR-10-LABX-0039-PALM) is also acknowledged.

Appendix

In the radiative heat transfer, a view factor $F_{1 \rightarrow 2}$ is the proportion of the radiative flux which leaves surface 1 and strikes a surface 2. We may use this geometrical factor in order to quantify approximately the 3D heating homogeneity of the plane target. Since the geometry is symmetrical (in practice it depends on the symmetry of the two heating beams), we need only to determine the radiation transfer from one sphere to one side of the tilted target. It is assumed that the radiation from the inner surface of the spheres is uniform. We then compute numerically the view factor between the inner surface S_1 of a sphere (accounting for the holes in it) and an elementary surface dS_2 at a given point of the target, using the expression below:

$$F_{S_1 \rightarrow dS_2} = \frac{dS_2}{S_1} \int_{S_1} \frac{\cos(\theta_1)\cos(\theta_2)}{\pi r^2} \Delta(\theta_1, \theta_2) dS_1$$

where θ_1 and θ_2 are the angles between the surface normal and a ray joining both differential areas, r is the distance between dS_1 and



dS_2 and $\Delta(\theta_1, \theta_2)$ is a blocking factor which accounts for the shadowing of the source surface by the cavity itself. The calculations are then mirrored in order to obtain an illumination map on each side of the plane target.

It is important to note that for Figs. 3 and 4, calculations are made with the quantity $F_{dS_2 \rightarrow S_1}$ and not with $F_{S_1 \rightarrow dS_2}$ to obtain more significant values. These two quantities are connected by the formula:

$$dS_2 F_{dS_2 \rightarrow S_1} = S_1 F_{S_1 \rightarrow dS_2}$$

References

- [1] P. Renaudin, C. Blancard, J. Bruneau, G. Faussurier, J.-E. Fuchs, S. Gary, J. Quant. Spectrosc. Radiat. Transfer 99 (2006) 511.
- [2] Y. Zhao, J. Yang, J. Zhang, J. Liu, X. Yuan, F. Jin, Rev. Sci. Instrum. 80 (2009) 043505.
- [3] C. Chenais-Popovics, Laser Part. Beams 20 (2002) 291.
- [4] C. Reverdin, F. Thais, G. Loisel, M. Bougeard, Rev. Sci. Instrum. 81 (2010) 10E327.
- [5] A. Ben-Kish, A. Fisher, E. Cheifetz, J.L. Schwob, Rev. Sci. Instrum. 71 (2000) 2651.
- [6] J.L. Bourgade, B. Villette, J.L. Bocher, J.Y. Boutin, S. Chiche, N. Dague, et al., Rev. Sci. Instrum. 72 (2001) 1173.
- [7] F. Gilleron, H. Merdji, M. Fajardo, O. Henrot, J.C. Gauthier, C. Chenais-Popovics, et al., J. Quant. Spectrosc. Radiat. Transfer 69 (2001) 217.
- [8] C.A. Back, L. Da Silva, H. Kornblum, D. Montgomery, B. MacGowan, G. Glendinning, et al., J. Quant. Spectrosc. Radiat. Transfer 51 (1994) 19.
- [9] (a) L.B. Da Silva, B.J. MacGowan, D.R. Kania, B.A. Hammel, C.A. Back, E. Hsieh, et al., Phys. Rev. Lett. 69 (1992) 438; (b) C. Chenais-Popovics, M. Fajardo, F. Gilleron, U. Teubner, J.-C. Gauthier, C. Bauche-Arnoult, et al., Phys. Rev. E. 65 (2001) 016413.
- [10] F. Thais, S. Bastiani, T. Blenski, C. Chenais-Popovics, K. Eidmann, W. Fölsner, et al., J. Quant. Spectrosc. Radiat. Transfer 81 (2003) 473.
- [11] G. Loisel, P. Arnault, S. Bastiani-Ceccotti, T. Blenski, T. Caillaud, J. Fariaut, et al., High Energy Density Phys. 5 (2009) 173.
- [12] G. Schurtz, R. Dautray, J.P. Watteau (Eds.), La fusion thermonucléaire par laser, part. 3, vol. 2, Eyrolles, Paris, 1993.
- [13] M. Busquet, Phys. Fluids B 5 (1993) 4191.
- [14] (a) C. Bowen, P. Kaiser, J. Quant. Spectrosc. Radiat. Transfer 81 (2003) 85; (b) C. Bowen, F. Wagon, D. Galmiche, P. Loiseau, E. Dattolo, D. Babonneau, Phys. Plasmas 11 (2004) 4641.
- [15] Q. Porcherot, J.-C. Pain, F. Gilleron, T. Blenski, High Energy Density Phys. 7 (2011) 234.
- [16] (a) J.-C. Pain, F. Gilleron, Q. Porcherot, T. Blenski, Proceedings of the 40th EPS Conference on Plasma Physics, P4.403. <<http://ocs.ciemat.es/EPS2013PAP/pdf/P4.403.pdf>>, 2013; (b) J.-C. Pain, F. Gilleron, T. Blenski, Laser Part. Beams 33 (2015) 201.
- [17] T. Blenski, A. Grimaldi, F. Perrot, J. Quant. Spectrosc. Radiat. Transfer 65 (2000) 91.
- [18] R.D. Cowan, The Theory of Atomic Structure and Spectra, University of California Press, Berkeley, 1981.
- [19] C.A. Iglesias, V. Sonnad, High Energy Density Phys. 8 (2012) 154.
- [20] J.-C. Pain, F. Gilleron, High Energy Density Phys. 15 (2015) 30.
- [21] T. Blenski, G. Loisel, M. Poirier, F. Thais, P. Arnault, T. Caillaud, et al., Phys. Rev. E 84 (2011) 036407.
- [22] T. Blenski, G. Loisel, M. Poirier, F. Thais, P. Arnault, T. Caillaud, et al., High Energy Density Phys. 7 (2011) 320.